Nano Energy 76 (2020) 105041

Contents lists available at ScienceDirect

Nano Energy

journal homepage: http://www.elsevier.com/locate/nanoen

A lithium-sulfur battery with a solution-mediated pathway operating under lean electrolyte conditions

Hui Wang [a,b], Yuyan Shao [a,b], Huilin Pan [a,b], Xuefei Feng [c], Ying Chen [a,d], Yi-Sheng Liu [c], Eric D. Walter [d], Mark H. Engelhard [e], Kee Sung Han [a,d], Tao Deng [b,f], Guoxi Ren [c], Dongping Lu [b], Xiaochuan Lu [b], Wu Xu [b], Chunsheng Wang [f], Jun Feng [c], Karl T. Mueller [a,d], Jinghua Guo [c], Kevin R. Zavadil [g], Ji-Guang Zhang [a,b,*]

[a] Joint Center for Energy Storage Research (JCESR), Pacific Northwest National Laboratory, Richland, WA, 99354, USA
[b] Energy & Environment Directorate, Pacific Northwest National Laboratory, Richland, WA, 99354, USA
[c] Advanced Light Source, Lawrence Berkeley National Laboratory, Berkeley, CA, 94720, USA
[d] Physical and Computational Sciences Directorate, Pacific Northwest National Laboratory, Richland, WA, 99354, USA
[e] Environmental Molecular Sciences Laboratory, Pacific Northwest National Laboratory, Richland, WA, 99354, USA
[f] Department of Chemical and Biomolecular Engineering, University of Maryland, College Park, MD, 20742, USA
[g] Joint Center for Energy Storage Research (JCESR), Sandia National Laboratories, PO BOX 5800, Albuquerque, NM, 87185, USA

ARTICLE INFO

Keywords:
Li-S batteries
Li2S4-Rich electrolyte
Solution-based pathway
High ionic-associationstrength anions
Lean electrolyte conditions

ABSTRACT

Lithium-sulfur (Li–S) battery is one of the most promising candidates for the next generation energy storage systems. However, several barriers, including polysulfide shuttle effect, the slow solid-solid surface reaction pathway in the lower discharge plateau, and corrosion of Li anode still limit its practical applications, especially under the lean electrolyte condition required for high energy density. Here, we propose a solution-mediated sulfur reduction pathway to improve the capacity and reversibility of the sulfur cathode. With this method, a high coulombic efficiency (99%) and stable cycle life over 100 cycles were achieved under application-relevant conditions (S loading: 6.2 mg cm^{-2}; electrolyte to sulfur ratio: 3 mL_E g_S^{-1}; sulfur weight ratio: 72 wt%). This result is enabled by a specially designed Li_2S_4-rich electrolyte, in which Li_2S is formed through a chemical disproportionation reaction instead of electrochemical routes. A single diglyme solvent was used to obtain electrolytes with the optimum range of Li_2S_4 concentration. Operando X-ray absorption spectroscopy confirms the solution pathway in a practical Li–S cell. This solution pathway not only introduces a new electrolyte regime for practical Li–S batteries, but also provides a new perspective for bypassing the inefficient surface pathway for other electrochemical processes.

1. Introduction

The development of rechargeable lithium-sulfur (Li–S) batteries based on conversion reactions is driven by their higher theoretical specific energy at reduced cost compared to those of Li-ion batteries based on intercalation reactions [1–6]. However, Li–S batteries still suffer from their limited cycle life and low specific energy under flooded electrolyte conditions. These challenges are related to the continuous irreversible passivation of electrode by insulation Li_2S and the deteriorating solid-electrolyte interphases on the Li metal anode upon cycling under high sulfur loadings [7–11]. To overcome these challenges and reach the full potentials of Li–S chemistry, it is essential to tune electrolyte formulations to enable a robust interface and a new reversible pathway for Li–S reactions [12–17].

Full sulfur-utilization has rarely been reported in solvent-flooded Li–S cells, where the traditional binary ether solvent of 1,3-dioxolane (DOL) and 1,2-dimethoxyethane (DME) are used [18,19]. Most of the reported specific capacity of sulfur cathode is less than 1200 mAh g^{-1} (i.e., 71.6% of sulfur utilization based on its theoretical capacity of 1672 mAh g^{-1}), limited by a surface pathway in the lower discharge plateau because the active surface area is decreasing during discharge [20]. Recently, a new strategy of sparingly solvating electrolytes has been proposed to render a significant increase in the sulfur utilization at elevated temperature owing to the increased concentration of $S_3^{\cdot-}$ radical

* Corresponding author. Joint Center for Energy Storage Research (JCESR), Pacific Northwest National Laboratory, Richland, WA, 99354, USA.
E-mail address: jiguang.zhang@pnnl.gov (J.-G. Zhang).

https://doi.org/10.1016/j.nanoen.2020.105041
Received 28 April 2020; Received in revised form 29 May 2020; Accepted 30 May 2020
Available online 30 June 2020

in a high dielectric constant (DC) solvent of acetonitrile, where a chemical/electrochemical redox pathway involving $S_3^{\bullet-}$ was proposed to take place simultaneously [21,22]. In other words, the full sulfur utilization enabled by this pathway strongly relies on the concentration of $S_3^{\bullet-}$ [23,24]. However, the poor compatibility of high DC solvents against Li metal has been an unsettled hurdle and the aggressive nucleophilic attack of DOL and carbonate solvents by $S_3^{\bullet-}$ has been extensively studied [25–27]. Fortunately, the Li-benign linear ether solvents, except for DME, have been experimentally confirmed to be resistant to $S_3^{\bullet-}$ attack [28,29]. Linear ethers with a higher number of solvating oxygen atoms are found to enhance the stability of the solvent-Li^+ solvating complex and thus the stability of $S_3^{\bullet-}$.

Li salts with different anions have been reported to greatly affect the solubility of low-order Li polysulfides (LiPS) and thus the concentration of $S_3^{\bullet-}$, since the latter is a product of the disproportionation reaction equilibrium of LiPS [30,31]. Higher ionic-association-strength (i.e., high Lewis basicity) of anion X^- ($X^- = NO_3^-$, $CF_3SO_3^-$, Br^-, etc.) has been demonstrated to render a higher concentration of low-order LiPS due to a stronger interaction between Li^+ from LiPS and X^-, compared to the low ionic-association-strength of the base anion of $N(CF_3SO_2)_2^-$ (bis (trifluoromethanesulfonyl)imide [$TFSI^-$]). One can thus expect that tuning electrolyte formulations, especially through highly solvating Li-benign linear ether solvents [12] and high ionic-association-strength anions, can steer a synergetic chemical/electrochemical sulfur redox pathway in the lower discharge plateau by the presence of stabilized $S_3^{\bullet-}$.

In this work, we report a solution-mediated chemical/electrochemical sulfur redox pathway, enabled by the optimal Li_2S_4 concentration in the electrolyte, to circumvent undesired solid charge-transfer process. We demonstrated that this new approach can boost the sulfur utilization and cyclability of Li–S batteries with high sulfur loadings (>6 mg cm^{-2}) under lean electrolyte conditions at room temperature. In particular, diglyme (G2) is employed to prepare an optimized high concentration of Li_2S_4 with the aid of NO_3^-. This Li_2S_4-retaining strategy is feasible to decouple the sulfur reduction pathway from both the bulk electrolyte and the electroactive surface area, to circumvent conventional solid-solid charge transfer in the lower discharge plateau, and to make reversible Li stripping/plating.

2. Results and discussion

2.1. A new Li_2S_4-dictated pathway under lean electrolyte conditions

In a Li–S cell with a critical electrolyte-to-sulfur (E/S) ratio (i.e., ≤4.0 mL_E g_s^{-1} when the maximum solubility of LiPS reaches 8 M [S]; where mL_E and g_s represent volume of electrolyte and weight of sulfur in Li–S cell, respectively, Supplementary Fig. 1), sulfur is first reduced at the cathode during discharge to form quasi-solid Li_2S_4 by reactions [1-2] as shown below [32]. In the subsequent reaction represented by the lower discharge plateau [3], nucleation and growth barriers of insulating solid Li_2S present a tremendous hurdle due to slow Li^+ diffusion and solid-solid charge-transfer process.

$$S_8\ (s) + 2Li^+ + 2e^- \rightarrow Li_2S_8\ (s\ or\ l) \quad (1)$$

$$Li_2S_8\ (s\ or\ l) + 2Li^+ + 2e^- \rightarrow 2Li_2S_4\ (s) \quad (2)$$

$$Li_2S_4\ (s) + 6Li^+ + 6e^- \rightarrow 4\ Li_2S\ (s) \quad (3)$$

E^{Θ}=2.1 V

In order to investigate electrolyte dependence of sulfur utilization in the lower discharge plateau under lean electrolyte conditions, selection of a carbonaceous model matrix is important to eliminate effects of the diffusion/migration of high-order LiPS in the bulk electrolytes from cathodes. A microporous sulfur-loading matrix of activated carbon fiber cloth (ACFC) was used as a model substrate (Supplementary Fig. 2) because it can confine high-order LiPS in micropores [13]. Despite different electrolytes and sulfur sources, no diffusion/migration of high-order LiPS from micropores of ACFC was observed in cyclic voltammograms (Supplementary Fig. 2). Moreover, the relatively high pore volume of ACFC allows high sulfur loadings in micropores with limited solvent permeation [13], akin to where the Li–S redox reactions would take place in practical applications.

A Li–S cell was assembled with a sulfur containing electrolyte E_G2_0.5 M Li_2S_4 (E_G2 represents 1 M LiTFSI_0.3 M $LiNO_3$ in G2) as the sulfur source and ACFC as the carbon matrix. Sulfur loading is 1.58 mg cm^{-2} calculated by total amount of sulfur in the electrolyte divided by the geometrical area of ACFC electrode. A typical discharge/charge curve is shown in Fig. 1a, which shows a discharge capacity of 1590 mAh g_s^{-1} and a coulombic efficiency (CE) of 99.1%, suggesting that 95.1% of the sulfur is reduced to solid Li_2S. To determine the sulfur reduction mechanism in E_G2_0.5 M Li_2S_4, potentiodynamic cycling with galvanostatic acceleration (PCGA) was performed in the Li|E_G2_0.5 M Li_2S_4|ACFC; results are shown in Fig. 1b. PCGA is a quasi-equilibrium technique that can provide very useful detailed information on electrochemical processes by analyzing the integral of the current during the step time (δQ) versus the potential in the same step. The reversibility of solid Li_2S_4 reduction at 2.06 V and oxidation at 2.22 V is high, as indicated by the observed comparable δQs and the narrow potential difference of 0.16 V between the two reactions, which further supports ACFC as a model material. Interestingly, there is an additional broad reduction peak below the major reduction. To reveal the origin of the broad reduction peak in the 1.98–1.99 V, the dependence of PCGA traces for the discharge of Li–S cell on Li_2S_4 concentrations and stepwise potentials was then investigated and the results are shown in Supplementary Fig. 3. A broad peak between 1.9 and 2 V was observed for the sample using a Li_2S_4 containing electrolyte (E_G2_0.5 M Li_2S_4). In contrast, no broad reduction peak was observed for the cell without Li_2S_4 (E_G2), indicating the strong dependence of this broad reduction peak on the electroactive species of Li_2S_4 (see Supplementary Fig. 3a). On the other hand, a sharp reduction peak, corresponding to the major electrochemical reduction of Li_2S_4 from bulk electrolyte, is observed at ~2.04 V and increases with increasing concentration of Li_2S_4. However, the subsequent broad reduction peak between 1.9 and 2 V is weakened, which is consistent with the stepwise potential dependence of PCGA measurement results using the same cell shown in Supplementary Fig. 3b. The size of this broad reduction peak is thus closely related to the Li_2S_4-retaining in the bulk electrolytes, suggesting a new reduction pathway for sulfur in micropores.

The cell using E_G2_0.5 M Li_2S_4 was cycled at the much lower rate of 0.075C; results are shown in Fig. 1c. A gradual increase in the discharge capacity was observed in the initial cycles probably due to the improved wetting ability of ACFC [33,34]. After the 10th cycle, both the maximum deliverable discharge capacity (i.e. 1590 mAh g_s^{-1}) and CE of the cell continuously decay upon further cycling, suggesting the sulfur redox environment significantly evolves within ACFC as soon as most sulfur from Li_2S_4 in bulk electrolytes migrates into ACFC and only sparse Li_2S_4 is remained outside ACFC. An identical cell discharged at 0.3 C showed an increasing discharge capacity from 825 to 979 mAh g_s^{-1} and an ultrahigh average CE of 99.7% for 100 cycles (Fig. 1c). During fast discharges, appropriately half of the Li_2S_4 (i.e., 0.25 M) remained outside the ACFC, assuming 100% sulfur utilization in micropores (Fig. 1a) at the delivered specific capacity of 836 mAh g_s^{-1}. Further, a new cell with E_G2_1.5 M Li_2S_4 (E_G2: 1 M LiTFSI_0.9 M $LiNO_3$ in G2) was deliberately discharged at 0.075C, as shown in Fig. 1d. This cell delivered a relatively high specific capacity of *ca.*1200 mAh g_s^{-1} and an average CE as high as 99.8%, compared to 96.9% for the cell using 0.5 M Li_2S_4. The Li_2S_4 remaining at the outside of ACFC is estimated to be 0.42 M in this cell during cycling. These results clearly suggest that Li_2S_4 remaining on the outside of the ACFC plays a special role in enabling a high sulfur utilization in the lower discharge plateau with limited solvents permeation (i.e. lean electrolyte conditions).

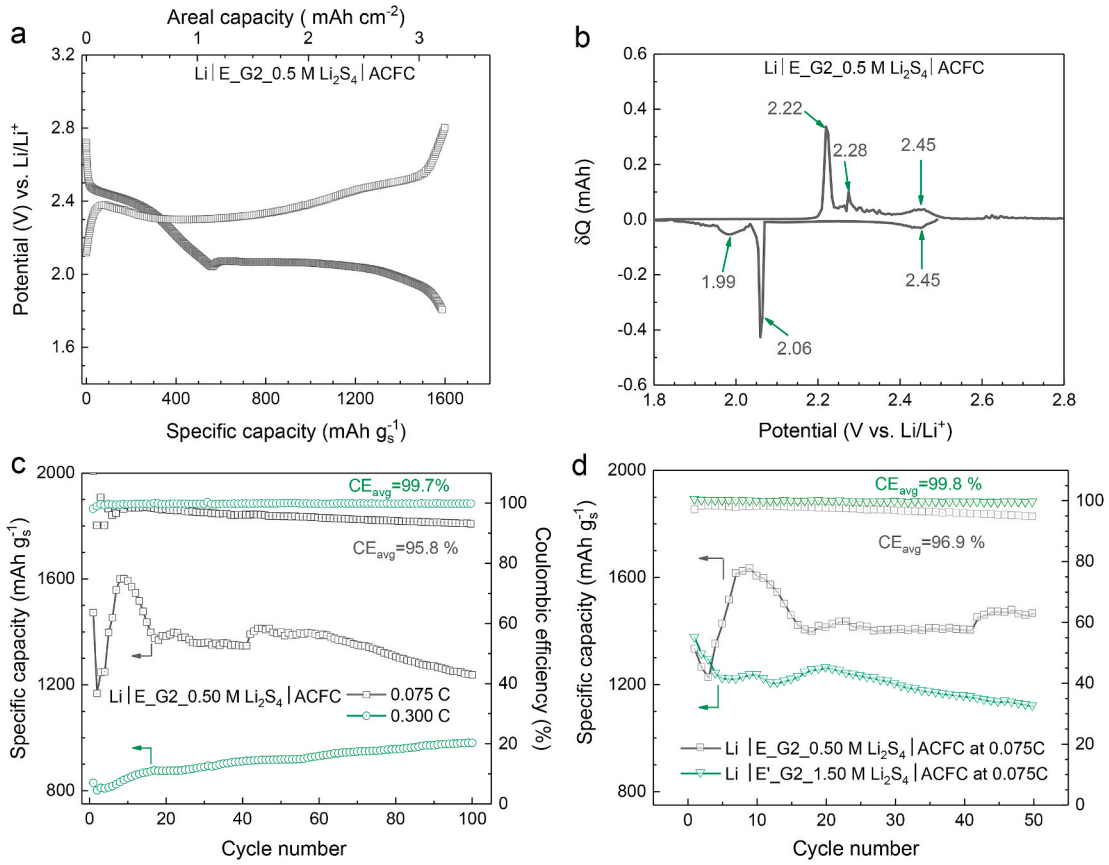

Fig. 1. A new Li_2S_4-dictated pathway under lean electrolyte conditions. (a) A typical discharge/charge curve of Li | E_G2_0.50 M Li_2S_4 | ACFC cell after initial cycles at 0.075 C and 30 °C; (b) PCGA trace of Li|E_G2_0.5 M Li_2S_4|ACFC at 30 °C. Retention degree of Li_2S_4 is tuned in the bulk electrolytes using various discharge rates for E_G2_0.5 M Li_2S_4 (c) and the same low discharge rate of 0.075C in different concentrations of Li_2S_4 (d); Fig. 1a is the 9th cycle curve of the Li–S cell in Fig. 1c at 0.075C. Microporous activated carbon fiber cloth (ACFC) was used as a model material to study electrolyte dependence of the sulfur reduction pathway under lean electrolyte conditions. Different concentrations of Li_2S_4 were prepared in E_G2 (1 M LiTFSI_0.3 M $LiNO_3$ in G2) and E_G2 (1 M LiTFSI_0.9 M $LiNO_3$ in G2).

We also compared the effect of different sulfur species loaded by different approaches on the performance of Li–S cells, with the same total sulfur loading (including those in electrode and electrolyte) and electrolytes volume. Three Li–S cells using ACFC were prepared as shown in Supplementary Fig. 4. In the Supplementary Figs. 4a–b, sulfur was introduced into ACFC prior to cell assembly (see Method section for details). In the Supplementary Fig. 4c, no sulfur presents in ACFC prior to cell assembly and all the sulfur in the cell originate from electrolyte. The electrolytes used in these three cells are base electrolyte-E_DOL/DME: 1 M LiTFSI_0.30 M $LiNO_3$ in DOL/DME (Supplementary Fig. 4b), E_G2 (Supplementary Fig. 4a), and E_G2_0.5 M Li_2S_4 (Supplementary Fig. 4c). All cells were tested at 0.3 C rate and 30 °C. After 500 cycles, the lower discharge plateau corresponding to reaction [3] totally disappeared and the capacity decay was almost continuous in the cells using E_G2 and E_DOL/DME, suggesting the surface pathway of reaction [3] should prevail in these two cells to result in a parasitic loss of surface area by the passivation of Li_2S during cycling. However, the length of the lower discharge plateau has a minimal change for the cell using E_G2_0.5 M Li_2S_4. This indicates that the presence of excess Li_2S_4 in the electrolyte is helpful to stabilize the lower discharge plateau during cycling.

2.2. *Dependence of sulfur utilization efficiency on the content of Li_2S_4 in electrolyte*

To further correlate the interplay between Li_2S_4 content in the bulk electrolyte and the reduction efficiency of solid Li_2S_4 under lean electrolyte conditions, ACFC_Li_2S_8 was prepared by preloading 30 μL of 1 M Li_2S_8 (sulfur mass loading: 6.06 mg cm^{-2}) into ACFC. Fig. 2a shows typical discharge curves of Li | E_G2_*x* M Li_2S_4 | ACFC_1 M Li_2S_8 with an E/S ratio of 3.0 $mL_E\ g^{-1}_{s\_cathode}$ at 0.12 mA cm^{-2} and 30 °C, where $g_{s\_cathode}$ represents the weight of sulfur in cathode (not including those in electrolyte). The achievable discharge capacity shows a strong correlation with the concentration of Li_2S_4 in the electrolyte. The cell using E_G2_0.5 M Li_2S_4 shows a significantly high capacity of 1520 mAh $g^{-1}_{s\_cathode}$ based on preloaded Li_2S_8 and1268 mA g^{-1}_{total} based on the total sulfur loading (including those pre-loaded in ACFC and those in the electrolyte) at an elevated discharge potential. In contrast, limited capacities of <400 mAh $g^{-1}_{s\_cathode}$ were observed for lower (<0.5 M) and higher concentrations (0.75 M) of Li_2S_4, indicating that an optimal concentration of Li_2S_4 in the bulk electrolytes is required to reduce preloaded Li_2S_8 to solid Li_2S_4 and the following Li_2S effectively. This is the first time that nearly 100% solid Li_2S_4 reduction has been reported for Li–S coin cells with high sulfur loadings and lean electrolytes.

Cells were both halted near the nucleation stage using the couple of E_G2|ACFC_Li_2S_8 or E_G2_0.50 M Li_2S_4|ACFC_S_8 in Fig. 2b and Supplementary Fig. 5 indicate that both the starting sulfur material and the 0.5 M Li_2S_4 content in electrolyte have a remarkable impact on the sulfur utilization. The cell using E_DOL/DME presents a lower discharge plateau, at 1.85 V, and a limited discharge capacity of 897 mAh $g^{-1}_{s\_cathode}$, far below that of the cell using E_G2_0.50 M Li_2S_4. Moreover, bulk electrolytes with 2 M [S] were made from 0.25 M Li_2S_8 and 0.33 M Li_2S_6 and examined, as shown in Fig. 2c. Interestingly, the cell using 0.33 M Li_2S_6 shows the absence of a lower discharge plateau. However, the cell using 0.25 M Li_2S_8 presents a specific capacity of 1884 mAh $g^{-1}_{s\_cathode}$, indicating that sulfur from the bulk electrolyte of 0.25 M Li_2S_8

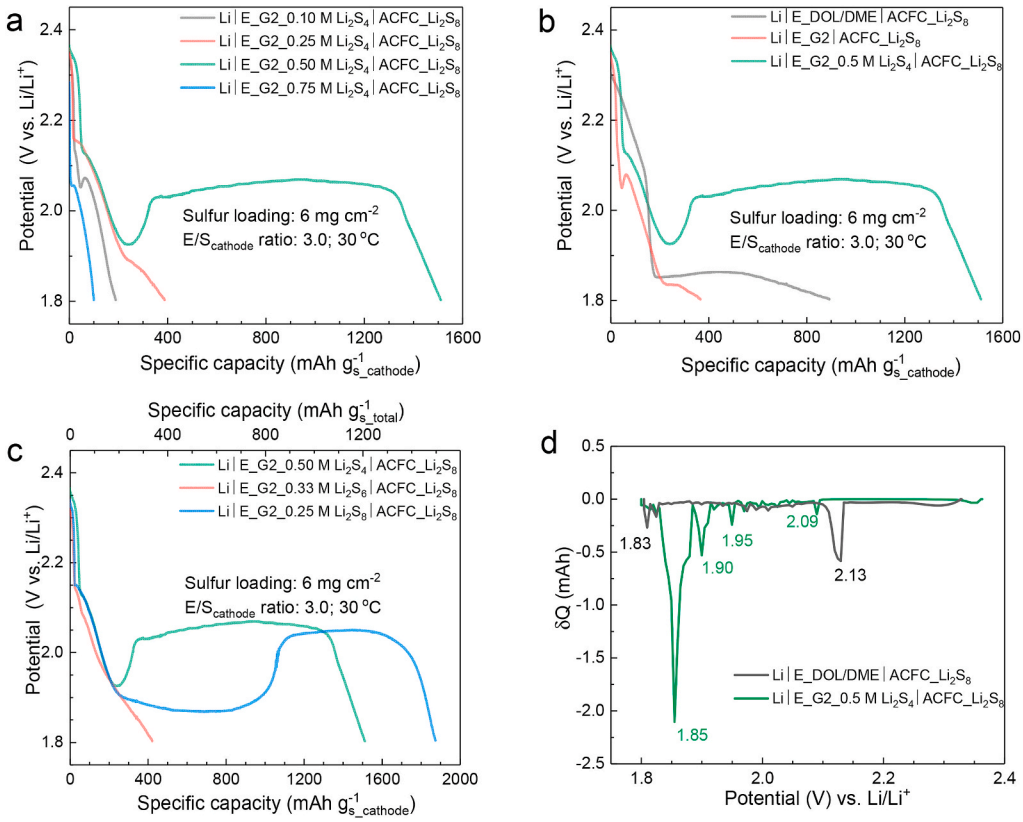

Fig. 2. Li_2S_4-retention dependence on sulfur utilization. Electrolyte dependence of the typical discharge capacity for Li–S cells using ACFC-Li_2S_8 as the cathode with a sulfur loading of 6 mg cm^{-2} at an $E/S_{cathode}$ ratio of 3.0 mL_E $g^{-1}_{S\_cathode}$, 0.12 mA cm^{-2}, and 30 °C. The $g_{s\_cathode}$ represents the weight of sulfur in cathode. (a) Using different concentrations of Li_2S_4 in E_G2; (b) using E_DOL/DME(1 M LiTFSI_0.3 M $LiNO_3$ in DOL/DME), E_G2, and E_G2_0.50 M Li_2S_4; (c) using different concentrations of LiPS with 2 M [S] in E_G2; (d) PCGA curves for the discharge of two Li–S cells with different electrolytes.

migrated into the ACFC and contributed to the total capacity due to the concurrent reduction of Li_2S_8 from the bulk electrolyte and the ACFC, where the intermediate reduced species of Li_2S_6 are not supposed to generate from E_G2_0.25 M Li_2S_8; otherwise, it would exhibit no lower discharge plateau, as did the cell using E_G2_0.33 M Li_2S_6.

Fig. 2d shows the discharge PCGA traces obtained from cells using E_DOL/DME and E_G2_0.50 M Li_2S_4. The PCGA trace of the cell using E_G2_0.50 M Li_2S_4 presented another unusual sulfur reduction pathway, where multiple discharge reactions are shown to take place at 2.09, 1.95, 1.90, and 1.85 V, respectively. It shows a continuously increasing incremental charge upon cathodic sweeping, with the maximum observed at 1.85 V. However, for the cell using E_DOL/DME, only two peaks were observed, at 2.13 V and 1.83 V, with a decreasing incremental charge upon cathodic sweeping, which further corroborates that Li_2S_4 retention can significantly affect the reduction pathway of sulfur species from high sulfur loadings under lean electrolyte conditions.

2.3. A solution-mediated chemical/electrochemical route

To explain the strong correlation between Li_2S_4 content in electrolyte and the ultrahigh sulfur utilization under lean electrolyte conditions, we propose a solution pathway enabled by Li_2S_4-mediated reaction (Fig. 3a) to divide reaction [3] into the following steps:

At the potential dip (i.e., the onset of Li_2S nucleation):

$$3S_4^{2-}\ (l) \leftrightarrow 2\ S_3^{\bullet-} + 2S_3^{2-}\ (l) \quad (4)$$

$$2S_3^{\bullet-} + 2e^- \rightarrow 2S_3^{2-}\ (l) \quad (5)$$

After the potential dip in the elevated discharge plateau:

$$S_3^{2-}\ (l) + Li_2S_4\ (s) \leftrightarrow Li_2S\ (s) + S_6^{2-}\ (l) \quad (6)$$

$$S_6^{2-}\ (l) + 2e^- \rightarrow 2S_3^{2-}\ (l) \quad (7)$$

E^{Θ}=2.3 V

The presence of optimal-concentration Li_2S_4 in the bulk electrolyte drives the chemical disproportionation reaction [4] toward $S_3^{\bullet-}$, which is further reduced to soluble S_3^{2-} by reaction [5] [24,28]. Reactions [4,5] have been investigated by *in-situ* ultraviolet–visible absorption spectroscopy and electron paramagnetic resonance (EPR) spectroscopy in a tetraglyme-based electrolyte [20,28]. The soluble S_3^{2-} from reaction [5] chemically reacts with quasi-solid Li_2S_4 (reaction [6]) and generate Li_2S precipitate and soluble S_6^{2-}; the soluble and replenishable S_6^{2-} is further reduced into soluble S_3^{2-} (reaction [7]) at a higher redox potential (i.e. E^{Θ}=2.3 V) [23] than reaction [3] (i.e. E^{Θ}=2.1 V) [5,35], which prevents further reduction of bulk Li_2S_4 on cathodes and leads to the voltage dip before the onset of the lower discharge plateau. The reduction efficiency of solid Li_2S_4 is thus not affected by the decreasing available surface area during single discharge, and could potentially reach 100% by reactions [6,7]. Fig. 2a shows that the optimal concentration of Li_2S_4, that can allow reactions [4–7] (i.e., the synergetic chemical/electrochemical reactions) to take place with a low energy barrier and an elevated discharge plateau, is 0.50 M (i.e., optimal concentration ratio of S_3^{2-}/S_6^{2-}). The solubility of Li_2S_4 was reported to be as low as 0.0625 M in DOL/DME [30].The low solubility of Li_2S_4 and the poor stability of $S_3^{\bullet-}$ in DME and DOL (i.e., low concentration ratio of S_3^{2-}/S_6^{2-}) [26,29] means the synergetic chemical/electrochemical reactions are not likely to take place in the DOL/DME-based electrolytes. This is evidenced by the lack of elevation of the lower discharge plateau and a much lower discharge specific capacity, as shown in Fig. 2b. Reaction [6] will not take place in a low concentration ratio of S_3^{2-}/S_6^{2-} (CS_3^{2-}/CS_6^{2-}) if the bulk electrolytes still contain S_6^{2-} when the cell discharges beyond reaction [2], as depicted in Fig. 3b and demonstrated in Fig. 2c, and if the bulk electrolytes contains low concentration of CS_3^{2-} originating from low concentration of CS_4^{2-} in Fig. 2a. Further, a higher concentration of Li_2S_4 is found to result in a substantial decrease of lithium cation diffusion coefficient by ^{7}Li PFG-NMR measurements (Supplementary Table 1) to maintain the charge neutrality and then decrease the local supply of S_3^{2-}.

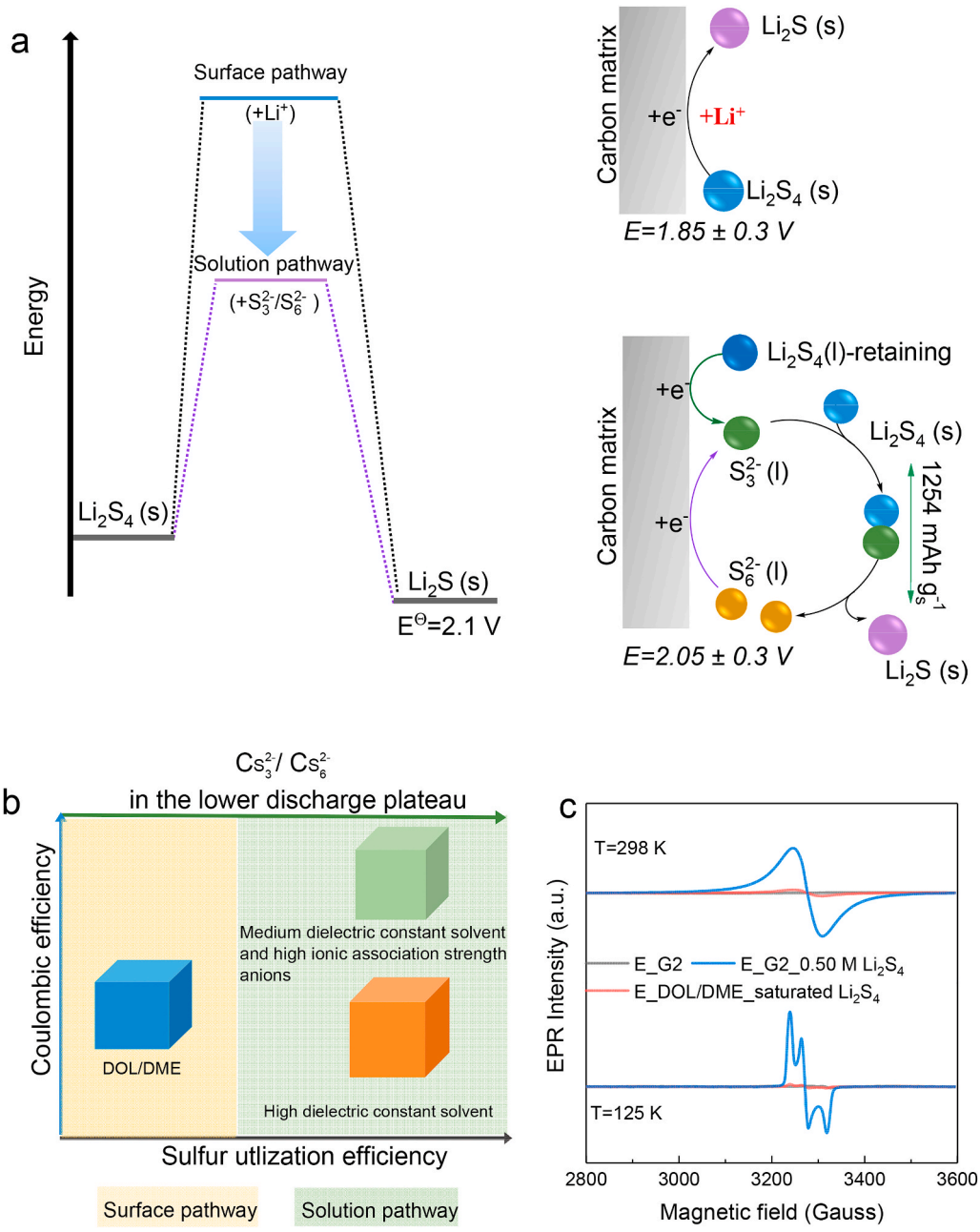

Fig. 3. Electrolyte dependence of sulfur discharge pathway. (a) Schematics of the effect of Li_2S_4-retaining solution pathway on the Gibbs free-energy plot at E^{Θ} for Li_2S_4 (s)/Li_2S (s) (left), and different pathways in the lower discharge plateau (right). S_6^{2-} is electrochemically reduced to S_3^{2-} at the carbon matrix surface, and then S_3^{2-} chemically reacts with solid Li_2S_4, producing solid Li_2S and itself being regenerated to S_6^{2-}. Initial S_3^{2-} comes from the reduction of S_4^{2-}-retaining in bulk electrolyte. As for the surface pathway, solid Li_2S_4 is electrochemically reduced with Li^+ to solid Li_2S with a higher overpotential at the carbon matrix surface; (b) Solvent and anion dependence of sulfur discharge pathway; (c) EPR spectra of E_G2, E_G2_0.5 M Li2S4 and E_DOL/DME_ saturated Li_2S_4 at 298 K (upper) and 125 K (lower).

To investigate the solvent-dependent of $S_3^{\cdot-}$ in electrolytes, non-invasive EPR measurements were performed for electrolytes of E_G2, E_G2_0.5 M Li_2S_4 and E_DOL/DME_saturated Li_2S_4 (images shown in Supplementary Fig. 6) in Fig. 3c. EPR spectrum at 125 K of E_G2_0.5 M Li_2S_4 clearly reveals the pattern of $S_3^{\cdot-}$ radical at g=2.034 [17,20], and the EPR spectrum also shows the persistent presence of the radical at room temperature (T=298 K). Similar pattern was not observed for E_G2 and greatly weakened for E_DOL/DME_saturated Li_2S_4. The concentration of $S_3^{\cdot-}$ radical is calculated to be 0, 0.6 mM, and 11.2 mM for E_G2, E_DOL/DME_saturated Li_2S_4 and E_G2_0.5 M Li_2S_4 respectively; the large difference in the concentration of $S_3^{\cdot-}$ clearly highlights the dramatic impact of solvents on the presence of $S_3^{\cdot-}$ and the resultant CS_3^{2-} that steers distinctive sulfur reduction pathway. Raman results further confirm the presence of $S_3^{\cdot-}$ in E_G2_0.5 M Li_2S_4 as shown in Supplementary Fig. 7, where a dominant and sharp peak of 534.6 cm^{-1} stemming from $S_3^{\cdot-}$ was observed [36].

2.4. Experimental verification of the Li_2S_4-enabled solution pathway

Since Li_2S_4 retention in the bulk electrolyte can drastically enhance the sulfur utilization under lean electrolyte conditions, it is very important to directly demonstrate whether or not Li_2S_4 plays a role in the proposed solution pathway. To demonstrate the occurrence of synergetic chemical/electrochemical reactions, operando sulfur K-edge X-ray absorption spectroscopy (XAS) was employed to probe sulfur speciation in a Li–S cells. Because the transmission of photon signal in XAS experiment is significantly attenuated by the thickness of the specimen, it is very difficult to obtain high quality signal when a thick ACFC (which comes from a commercial source with a fixed thickness) is used as the cathode host in Li–S cells. Therefore, an electrospun carbon fiber (ECF) with 1/5 of the thickness of ACFC is prepared and used as the cathode host in Li–S cells for operando study of the sulfur reduction pathway, where E_G2_0.5 M Li_2S_4 was used as the bulk electrolyte. It is worth to note that the electrolytes, not the carbon host, plays a

predominant role in the sulfur reduction pathway [34,37].

Fig. 4a and b shows XAS contours collected from Li–S cells using E_G2 and E_G2_0.5 M Li_2S_4 at ambient temperature, respectively. Piling-up XAS spectra of each cell are shown in Fig. 4c and d. The intermediate states of polysulfides are supposed to be identified by the ratio between the pre-peak at 2470.2 eV (characteristic pre-peak for polysulfides) and the main peak at 2472 eV (typical peak for elemental sulfur), since the relative intensity of the pre-peak is proportional to the relative amount of Li in Li_2S_x (Supplementary Table 2). The starting material of Li_2S_8 (x = 0.25 in Li_xS) in both operando XAS measurements (See Fig. 4a and b) was discharged from 0.25 to 0.50. Li–S cells have been reported to be prematurely terminated during this stage due to the rapid drop in the cell potential resulting from the sluggish solid-solid charge-transfer reaction [3] under lean electrolyte reactions. Wujcik et al. [38]reported the XAS evolution of a solid Li–S battery with a limited x range in Li_xS from 0 to 0.15 in a thick sulfur cathode, where the ratio of main peak to pre-peak area is continuously decreasing (i.e. the evolution from long Li_2S_x to short Li_2S_x) upon discharging, along with a prematurely cell potential failure. In the ether-based electrolytes for the x range from 0.25 to 0.50, the trend of decreasing concentration of $[S_6^{2-}]$ and increasing concentration $[S_4^{2-}]$ has been demonstrated by previous Li–S XAS studies [39,40], along with a continuously decrease in the cell potential. Here, the operando XAS cell of Li|E_G2|ECF_Li_2S_8 shows resembling phenomena in terms of the continuously decreases in the ratio of the main peak to pre-peak area (i.e. from long Li_2S_X to short Li_2S_x) and in the discharge cell potential in Fig. 4e. The ratio of the main peak to pre-peak area decreases from 7.0 to 3.0 in the x range from 0.25 to 0.43. In contrast, a distinct increase in the ratio of the main peak to the pre-peak area, i.e., an evolution from short Li_2S_x to long Li_2S_x, is observed from 2.8 to 5.1 in the x range from 0.32 to 0.46 for the operando XAS cell using E_G2_0.50 Li_2S_4 in Fig. 4f. In this discharge stage, the elevation of the discharge potential is observed as well. Increases in the peak area ratio and discharge cell potential can be regarded as a strong evidence of the Li_2S_x evolution from Li_2S_4 to Li_2S_6 in the bulk electrolyte for this operando cell, which thus strongly corroborate the proposed reactions of [4–7].

In a parallel experiment using the XAS cell of Li|E_G2_0.5 M Li_2S_4|ECF_Li_2S_8 (sulfur loading: >6 mg cm^{-2}; $E/S_{cathode}$ ratio: 3.0), the final solid discharge product was harvested when the cell was terminated discharging at 1431 mAh $g_{s\_cathode}^{-1}$ (x=1.99) to characterize its composition by ex-situ X-ray photoelectron spectroscopy (XPS) measurement as shown in Supplementary Fig. 8a. The dominant final solid product can be determined as Li_2S by corresponding fitted peaks of S_{2p} [41,42] as shown in Supplementary Fig. 8b and quantitative calculation with an accuracy of 96.5% in Supplementary Table 3.

2.5. Application of the Li_2S_4-enabled solution pathway

In this work, advantages of Li_2S_4 content in bulk electrolytes have been demonstrated (Fig. 1d and Supplementary Fig. 4), in terms of steering the synergetic chemical/electrochemical reactions (Fig. 4) and high compatibility with Li metal (discussed in the Supplementary Notes and shown in Supplementary Figs. 9–13. Li–S cells with high sulfur loadings under lean electrolyte conditions are expected to deliver a high specific capacity and long cycle life if the cell were just cycled between Li_2S_4 and Li_2S, with a theoretical capacity of 1254 mAh g_s^{-1}, by the Li_2S_4-retaining solution pathway.

ACFC was initially used as a model material to study the electrolyte-dependent sulfur reduction pathway under lean electrolyte conditions. Surprisingly, even Li–S cells using ACFC are fully charged at 2.8 V, where the retained Li_2S_4 might be oxidized into Li_2S_8 or migrate toward the Li metal anode with Li^+ owing to the stronger interaction between Li^+ and short-order LiPS [43], high sulfur utilization and CE are still maintained as observed in Fig. 1. This indicates that Li_2S_4, not the intermediate Li_2S_6, is always generated from the reduction of Li_2S_8 in G2; the resultant Li_2S_4 steers the solution pathway in ACFC. Supplementary Fig. 14 shows the cycling performance of Li|E'_G2_1.5 M Li_2S_4|ACFC with a high sulfur loading of 7.6 mg cm^{-2} at 1/30C (i.e., 0.42 mA cm^{-2})

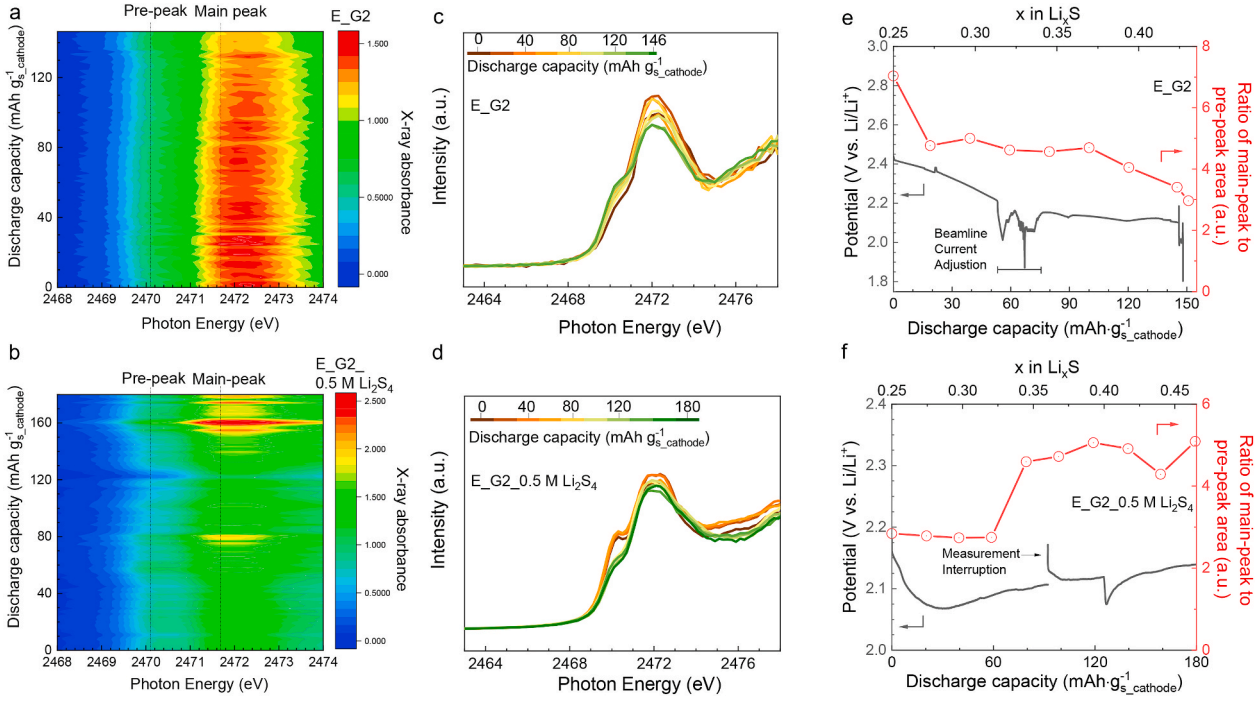

Fig. 4. Experimental corroboration of the Li_2S_4-retaining solution pathway. Normalized operando X-ray absorption spectroscopy (XAS) contours at the sulfur K-edge for (a) Li | E_G2 | ECF_Li_2S_8 (sulfur loading: 6 mg cm^{-2}; applied current density: 0.08 mA cm^{-2}) and (b) Li | E_G2_ Li_2S_4 | ECF_Li_2S_8 (sulfur loading: 4.3 mg cm^{-2}; applied current density: 0.04 mA cm^{-2}) upon initial discharge using electrospun carbon fiber (ECF) as the carbon matrix at an $E/S_{cathode}$ ratio of 3.0 mL_E $g_{S\_cathode}^{-1}$ and ambient temperature; (c–d) the piling-up XAS spectra for the operando XAS cells of Li|E_G2|ECF_Li_2S_8 and Li|E_G2_ Li_2S_4|ECF_Li_2S_8 every 40 mAh $g_{s\_cathode}^{-1}$ until x = 0.50; (e–f) operando discharge curves of XAS Li–S cells and corresponding analysis between x in Li_xS and the ratio of main peak to pre-peak area.

for discharging, and 1/7.5C for charging in the range 1.80–2.80 V. The E/S ratio was determined to be 5.20. The potential dip is greatly alleviated, even though the cell was charged to 2.8 V. Moreover, both excellent cycling retention and high CE can be achieved with a stable areal capacity of *ca.* 6 mAh cm^{-2}. Impact of the charge cut-off potential of Li|E_G2_1.5 M Li_2S_4|ACFC on the middle discharge potential (i.e. an indication of cell cycling retention and the sustainability of solution-mediated pathway) was investigated for 20 cycles with the same charge/discharge rate of 1/30 C at 30 °C as shown in Supplementary Fig. 15. Two different charge cut-off potentials of 2.63 V (i.e. oxidation to Li_2S_8) and 2.48 V (i.e. roughly oxidation to Li_2S_4) were selected based on CV measurement of this cell (Supplementary Fig. 16a). The cell terminated at 2.48 V showed a stable middle discharge potential, but the cell terminated at 2.63 V showed a rapid decrease in the middle discharge potential, indicating the solution pathway is highly sustained when the charge cut-off potential is carefully tuned to terminate the cell charge to the stage of Li_2S_4.

To demonstrate the general application of the Li_2S_4-enabled solution pathway, Electrospun carbon fiber (ECF) has been used to replace ACFC as sulfur-loading substrate because ECF is a typical macroporous carbon matrix which cannot prevent diffusion of high-order LiPS (i.e., soluble S_6^{2-} in reaction [6]) into electrolytes, and thus can be used to verify the Li_2S_4-enabled solution pathway. The Li| E_G2_0.5 M Li_2S_4|ECF_Li_2S_8 cell was cycled with a high sulfur loading of 6.2 mg cm^{-2} at an $E/S_{cathode}$ ratio of 3.0, 0.20 mA cm^{-2}, and 30 °C in the range 1.80–2.45 V, as shown in Fig. 5. The low charge cutoff potential of 2.45 V was deliberately chosen to prevent the oxidation of high-order LiPS into S_8 on the ECF and the migration of high-order LiPS toward Li (Supplementary Fig. 16) [44]. The Li–S cell shows potential-vs.-capacity curves resembling those of the Li|E_G2_0.5 M Li_2S_4|ACFC_Li_2S_8 cell (Fig. 2). The presence of Li_2S_4 can be signified by the continuous potential dip at approximately 50 mAh $g^{-1}_{s\_cathode}$ and by the high average CE of 99.0% upon cycling. It is thus reasonable to postulate that the Li_2S_4-enabled solution pathway prevails in this Li–S cell. The initial discharge capacity is lower than that observed using ACFC, probably due to the capacity loss from uncontrollable diffusion of S_6^{2-}. After 100 cycles, the cell can sustain the lower discharge plateau and deliver a specific capacity as high as 518 mAh g^{-1} based on Li_2S_8 preloaded in ECF cathode and 328 mAh g^{-1} based on the total sulfur from cathode and 0.5 M Li_2S_4 in electrolyte. The over-voltage in the initial stage of the discharge curve is related to the activation energy required to trigger reactions of [6,7]. These reactions are associated with the local diffusion of the species [S_3^{2-}] and [S_6^{2-}]. In other words, variation in local pore structure of the carbon matrix may affect the diffusion rate of [S_3^{2-}] and [S_6^{2-}] and associated over-voltage in the discharge curve.

Very few Li–S coin cells have been reported so far to survive for more than 40 cycles, with the continuous presence of the discharge plateau under similar conditions. The kinetics of the Li–S cell can be further improved by incorporation of a smart material (i.e., possessing high electronic conductivity and high Li^+ transport) into the carbon matrix under lean electrolyte conditions [45].

In summary, a solution-mediated pathway for sulfur reduction embracing synergetic chemical and electrochemical processes is described in Li–S cells with high sulfur loadings under lean electrolyte conditions. Excellent cycling performance of prototype Li–S cells validates the feasibility of developing practical Li–S cells using the Li_2S_4-retaining strategy.

3. Methods

3.1. Electrolyte preparation

The typical electrolyte formulation of 1 M LiTFSI_0.30 M Li nitrate ($LiNO_3$)_0.5 M Li_2S_4 in G2 was prepared as follows in an argon-filled glove box: $LiNO_3$ (99.99%, Sigma-Aldrich) was first added to G2 (99.5%, Sigma-Aldrich) under stirring for 4 h at room temperature. Stoichiometric amounts of Li_2S (99.98%, Sigma-Aldrich) and S (99.5%, Alfa Aesar) were then added into this transparent solution and heated with vigorous stirring for 48 h at 80 °C. A homogeneous, dark-red solution was then obtained. LiTFSI was finally added to the as-obtained red solution with stirring for 4 h at 80 °C. The same method was applied to prepare E_G2_0.5 M Li_2S_4 and E_DOL/DME_saturated Li_2S_4, except added solvents. When the concentration of Li_2S_4 increased to 1.50 M, the concentration of $LiNO_3$ was correspondingly increased to 0.90 M. LiTFSI and $LiNO_3$ were dried for four days under vacuum at 120 °C, and the G2 was dried over activated 3 Å molecular sieves in a glovebox prior to usage. Battery-grade DME (Gotion) and DOL (Gotion) were directly used as received to prepare the base electrolyte (E_DOL/DME) of 1 M LiTFSI_0.3 M $LiNO_3$ in DOL:DME (1:1 vol%).

3.2. Materials preparation

The ACFC_S_8 cathode was prepared by the adsorptive impregnation method described in our recent study[11]. CH700-20-type ACFC (pore

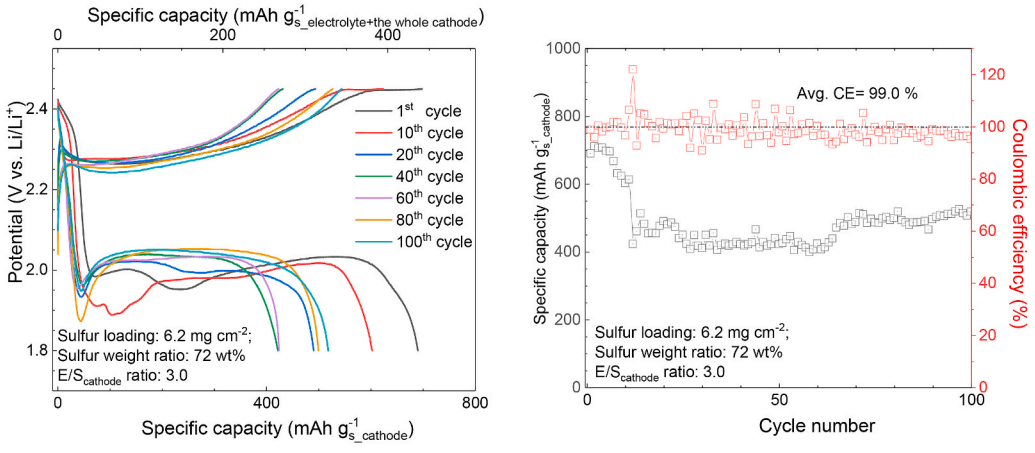

Fig. 5. Application of the Li_2S_4-retaining solution pathway in a different carbon matrix-ECF. Voltage profiles vs. capacity (a) and cycling capacity retention and coulombic efficiency (b) of Li | E_G2_0.5 M Li_2S_4 | ECF_Li_2S_8 cell with a sulfur loading of 6.2 mg cm^{-2} at an $E/S_{cathode}$ ratio of 3.0 mL_E $g^{-1}_{S\_cathode}$, 0.20 mA cm^{-2}, and 30 °C in the range 1.80–2.45 V.

volume: 0.878 cm^3 g^{-1}; pore size: ≤ 2 nm; Brunauer-Emmet-Teller (BET) surface area: 1635 m^2 g^{-1}; pore-clogged surface area: <10 m^2 g^{-1}; thickness: ca. 500 μm) from Kuraray Co., Ltd, Japan, was employed as a model material, with a practical sulfur loading range of 6–8.5 mg cm^{-2}, to study electrolyte dependence of sulfur redox chemistry under lean electrolyte conditions. The ACFC_Li_2S_8 cathode was prepared by drop-casting a solution of 1 M Li_2S_8 in DME. The solution was prepared by dissolving 0.01 mol of Li (200 μm thick, MTI Corporation) and 0.04 mol of sulfur (99.5%, Alfa Aesar) in 5 mL of DME (battery grade, BASF) solution in a hermetically sealed glass vial at 80 °C. The prepared solution was stirred for about 18 h until a dark-red, homogeneous solution was obtained. Different volumes (20–30 μL) of this mixture were dropped directly onto ACFC with a digital micropipette (Nichipet EX II 100, 10–100 μL, Nichiryo Co., Ltd.), and the DME solvent was allowed to evaporate at 120 °C under vacuum. The final amount of sulfur loading was controlled within the ACFC in the range of 4–6.5 mg cm^{-2}.

ECF was fabricated by electrospinning. Polyacrylonitrile (average MW 150,000, Sigma-Aldrich) and polymethylmethacrylate (MW = 120 000, Sigma-Aldrich) were dispersed at a 5:1 wt% ratio in anhydrous N, *N*-dimethylformamide (Sigma-Aldrich) and magnetically stirred for 20 h at 80 °C. Vacuum-dried silica nanoparticles (12 nm, LUDOX HS-30 colloidal silica, 30 wt% suspension in water, Sigma-Aldrich) were then added to this solution 2 wt %at a time. The as-prepared solution was fed through a syringe needle (BD 10 mL syringe, Luer-Lok tip) with the aid of an infusion syringe pump (78–0100C, Cole Parmer Instrument company, USA) at a constant flow rate of 1.20 mL h^{-1} and a DC voltage of 15 kV. The distance between the needle and the collector was 15 cm. The polymer composite membranes were stabilized in air at 250 °C for 1 h and subsequently carbonized at 700 °C for 3 h under Ar/H_2 flow (96:4, 100 cc min^{-1}). The membrane thickness ranged from 100 to 250 μm, and the mass loading was between 1.4 and 3.0 mg cm^{-2}. ECF-Li_2S_8 cathodes were prepared in the same way as ACFC_Li_2S_8 to assemble the Li–S cell. In the operando XAS measurement, SiO_2 was not added for the thin specimen of ECF_Li_2S_8.

3.3. Materials characterization

XPS measurements were performed with a Physical Electronics Quantera scanning X-ray microprobe. This system uses a focused, monochromatic, Al Kα X-ray (1486.7 eV) source for excitation and a spherical section analyzer. The instrument has a 32-element multichannel detection system. The X-ray beam is incident normal to the sample, and the photoelectron detector is at 45° off normal. High energy resolution spectra were collected using a pass energy of 69.0 eV with a step size of 0.125 eV. For the Ag 3d5/2 line, these conditions produced a full width at half maximum of 0.92 eV ± 0.05 eV. The binding energy scale was calibrated using the Cu 2p3/2 feature at 932.62 ± 0.05 eV and that of Au 4f7/2 at 83.96 ± 0.05 eV. All samples were rinsed with DME several times to remove residual electrolyte and then dried under vacuum for 20 min. To avoid side reactions or electrode contamination with ambient oxygen and moisture, electrodeposited Li was transported from the glovebox to the XPS and scanning electron microscope (SEM) instruments in a hermetically sealed container filled with Ar. The morphology of Li electrodeposited onto Cu was investigated using a Quanta focused-ion-beam SEM (FEI, Quanta 650 ESEM).

All EPR measurements were performed on a Bruker ELEXSYS E580 spectrometer at both 298 K and 125 K. All samples were prepared inside a glove box filled with nitrogen immediately before EPR experiments to minimize the influence of air and moisture. For liquid samples, a capillary with ID 0.8 mm and OD 1 mm was used to hold the solution in the EPR cavity with both ends sealed by Critoseal™ Leica Microsystems capillary tube sealant; the capillary was further placed inside a 4 mm EPR tube with the open end sealed inside a glove box. The typical settings for the spectra were microwave frequency = 9.32 GHz, sweep width = 1000 G, sweep time = 42 s, time constant = 40.96 ms, power = 20 mW, field modulation amplitude = 15 G. Absolute spin concentrations of the samples were determined by calibration curves of the spin standard TEMPO (2,2,6,6-tetramethyl-1-piperidinyloxyl) with concentrations varying from 0.01 mM to 100 mM.

Lithium cation diffusion coefficient (D_{Li}) of the range of samples was determined by ^{7}Li pulsed field gradient (PFG) NMR measurement at Larmor frequency of 2π × 232.98 rad MHz at 20 °C using a 14.1 T (600 MHz ^{1}H) NMR spectrometer (Agilent, USA) equipped with a 5 mm z-gradient probe (Doty Scientific, USA), which can generate a maximum gradient strength of ~31 T/m. The echo height, S(*g*), recorded as a function of gradient strength, *g*, was fitted with the Stejskal-Tanner equation [46].

$$S(g) = S(0)e^{\left[-D(\gamma g\delta)^2\left(\Delta-\frac{\delta}{3}\right)\right]} \quad (8)$$

where S(*g*) and S(0) are the echo heights at the gradient strengths of *g* and 0, respectively, *D* is the diffusion coefficient, γ is ^{7}Li gyromagnetic ratio, Δ is the time interval between the two gradient pulses, i.e. diffusion delay, and δ is the gradient length. The PFG-echo profiles were obtained using the stimulated echo sequence employing the bipolar gradient pulses (Dbppste, a vender supplied sequence, Agilent, USA) as a function of gradient strength varied with 16 equal steps. The maximum gradient strength was chosen according to the echo height at the maximum gradient strength. The 90° pulse length, Δ and δ were 8 μs, 30 and 2 ms, respectively.

Micro-Raman measurements were performed using a 633 nm laser source, which was attenuated using a variable neutral density filter wheel (to 25 μW/μm^2), reflected off a dichroic beam splitter, and focused onto the sample using a 10X air objective. Our commercial Raman microscope is based on an inverted optical microscope (Nikon Ti-E) coupled to a Raman spectrometer (Horiba LabRAM HR). The back-scattered light is collected through the same objective, transmitted through the beam splitter cube, and dispersed through a 600 l/mm grating. The effective resolution of the instrument in 3 cm^{-1} using this configuration.

3.4. Operando X-ray absorption spectroscopy measurements

Li–S battery cells of Li|Z_0.5 M Li_2S_4|ECF_Li_2S_8 were assembled in specially prepared CR2032 coin-cell cases. The cathode case was punched with a rectangular hole of 2 mm (horizontal) × 1 mm (vertical) at the center and tightly patched using 7 μm-thick Kapton tape, which has X-ray transmission of ~81% at 2470 eV). After assembly, no electrolyte leakage was observed. Li–S cells were tightly sealed in an aluminum foil envelope and then shipped to the Advanced Light Source (ALS), Lawrence Berkeley National Laboratory for the XAS measurements.

The *operando* XAS experiments were performed at Beamline 10.3.2 and 5.3.1 at the ALS. The X-ray beam size was 8 μm (horizontal) × 5 μm (vertical). The XAS spectra were collected in partial fluorescence-yield mode and calibrated using elemental sulfur spectra. All the S K-edge XAS spectra were collected under constant helium gas flow in a small chamber in front of the cell, and were acquired continuously during the discharging process. The peak position of the spectrum was calibrated relative to the sharp main peak of Na_2SO_4 reference sample. After subtracting the background, all the spectra intensities were normalized by taking the post-edge of S K-edge (the average of 2515–2520 eV).

3.5. Electrochemical measurements

The electrochemical characteristics of Li–S cells were investigated by PCGA, which is a common technique for characterization of electrochemical processes. In our case, PCGA was carried out by setting stepwise potential scans of 5 mV with a minimum current limit of 50 μA at 30 °C, using a Bio-Logic Instruments VSP potentiostat. The charge increment (δQ) was calculated by time integration of the current. Cyclic

voltammetry measurements of Li–S cells were conducted at a scan rate of 0.2 mV s^{-1} in the range of 1.8–2.8 V at 30 °C.

Cathodes were punched into 1.267 cm^2 diameter disks and weighed to acquire the accurate sulfur loading for each piece. Added volume of electrolytes was determined by the sulfur loading, based on the E/S ratios, with a digital micropipette (Nichipet EX II 100, 10–100 μL, Nichiryo Co., Ltd.). Half-cells with 200 μm thick Li metal foil (MTI Corporation) as the anode and polyethylene (Asahi Kasai, Japan) as the separator were assembled using CR2032 coin cells in an MBraun LABmaster glove box with an Ar atmosphere (<1 ppm O_2 and <1 ppm H_2O). In the Li||Cu cell without the polyethylene separator, a thin polypropylene spacer r with a central hole was used to eliminate effects of a separator and crimping pressure on the morphology of Li electrodeposits. The galvanostatic discharge/charge cycles were tested using a LANHE battery tester in an incubator at 30 °C.

Data availability

Data supporting the finds of this study are available within the paper and its Supplementary Information file, and are available from the corresponding author upon reasonable request.

Declaration of competing interest

The authors declare that they have no known competing financial interests or personal relationships that could have appeared to influence the work reported in this paper.

CRediT authorship contribution statement

Hui Wang: Conceptualization, Writing - original draft, Writing - review & editing. **Yuyan Shao:** Writing - original draft, Writing - review & editing. **Huilin Pan:** Writing - original draft, Writing - review & editing. **Xuefei Feng:** Formal analysis. **Ying Chen:** Formal analysis. **Yi-Sheng Liu:** Resources. **Eric D. Walter:** Formal analysis. **Mark H. Engelhard:** Formal analysis. **Kee Sung Han:** Formal analysis. **Tao Deng:** Investigation. **Guoxi Ren:** Investigation. **Dongping Lu:** Investigation. **Xiaochuan Lu:** Investigation. **Wu Xu:** Investigation. **Chunsheng Wang:** Investigation. **Jun Feng:** Investigation. **Karl T. Mueller:** Resources. **Jinghua Guo:** Formal analysis. **Kevin R. Zavadil:** Formal analysis. **Ji-Guang Zhang:** Conceptualization, Writing - original draft, Writing - review & editing.

Acknowledgements

This work was supported as part of the Joint Center for Energy Storage Research, an Energy Innovation Hub funded by the U.S. Department of Energy (DOE), Office of Science, Basic Energy Sciences. Authors thank Dr. Nathan Canfield and Dr. Haiping Jia for SEM characterizations., Dr. Xiaolin Li for help on electrospinning setup, and Dr. Patrick Z El Khoury for help on Raman characterization. ACFC samples were kindly supplied by the Carbon Materials Division of Kuraray Co., Ltd, Japan. The depth-profile XPS measurements were performed at the Environmental Molecular Sciences Laboratory (EMSL), a national scientific user facility sponsored by the DOE Office of Biological and Environmental Research and located at Pacific Northwest National Laboratory. The operando XAS work at Advanced Light Source of Lawrence Berkeley National Laboratory was supported by the Director of the Office of Science, Office of Basic Energy Sciences, of DOE under contract no. DEAC02-05CH1123. We thank Dr. Sirine Fakra for her technical support at the beamline.

Appendix A. Supplementary data

Supplementary data to this article can be found online at https://doi.org/10.1016/j.nanoen.2020.105041.

References

[1] D. Larcher, J.M. Tarascon, Nat. Chem. 7 (2014) 19.
[2] D. Eroglu, K.R. Zavadil, K.G. Gallagher, J. Electrochem. Soc. 162 (2015) A982–A990.
[3] B.D. McCloskey, J. Phys. Chem. Lett. 6 (2015) 4581–4588.
[4] P.G. Bruce, S.A. Freunberger, L.J. Hardwick, J.-M. Tarascon, Nat. Mater. 11 (2011) 19.
[5] H. Pan, J. Chen, R. Cao, V. Murugesan, N.N. Rajput, K.S. Han, K. Persson, L. Estevez, M.H. Engelhard, J.-G. Zhang, K.T. Mueller, Y. Cui, Y. Shao, J. Liu, Nat. Energy 2 (2017) 813–820.
[6] J. Chen, W.A. Henderson, H. Pan, B.R. Perdue, R. Cao, J.Z. Hu, C. Wan, K.S. Han, K. T. Mueller, J.-G. Zhang, Y. Shao, J. Liu, Nano Lett. 17 (2017) 3061–3067.
[7] X.-B. Cheng, J.-Q. Huang, Q. Zhang, J. Electrochem. Soc. 165 (2018) A6058–A6072.
[8] J. Yan, X. Liu, B. Li, Adv. Sci. 3 (2016), 1600101.
[9] Q. Pang, X. Liang, C.Y. Kwok, J. Kulisch, L.F. Nazar, Adv. Energy Mater. 7 (2017), 1601630.
[10] Y. Yuan, G. Tan, J. Wen, J. Lu, L. Ma, C. Liu, X. Zuo, R. Shahbazian-Yassar, T. Wu, K. Amine, Adv. Funct. Mater. 28 (2018), 1706443.
[11] Y. Yuan, J. Lu, Carbon Energy 1 (2019) 8–12.
[12] Q. Pang, A. Shyamsunder, B. Narayanan, C.Y. Kwok, L.A. Curtiss, L.F. Nazar, Nat. Energy 3 (2018) 783–791.
[13] H. Wang, B.D. Adams, H. Pan, L. Zhang, K.S. Han, L. Estevez, D. Lu, H. Jia, J. Feng, J. Guo, K.R. Zavadil, Y. Shao, J.-G. Zhang, Adv. Energy Mater. 8 (2018), 1800590.
[14] C. Shen, J. Xie, M. Zhang, P. Andrei, M. Hendrickson, E.J. Plichta, J.P. Zheng, Electrochim. Acta 248 (2017) 90–97.
[15] W. Li, H. Yao, K. Yan, G. Zheng, Z. Liang, Y.-M. Chiang, Y. Cui, Nat. Commun. 6 (2015) 7436.
[16] K. Dokko, N. Tachikawa, K. Yamauchi, M. Tsuchiya, A. Yamazaki, E. Takashima, J.-W. Park, K. Ueno, S. Seki, N. Serizawa, M. Watanabe, J. Electrochem. Soc. 160 (2013) A1304–A1310.
[17] Q. Wang, J. Zheng, E. Walter, H. Pan, D. Lv, P. Zuo, H. Chen, Z.D. Deng, B.Y. Liaw, X. Yu, X. Yang, J.-G. Zhang, J. Liu, J. Xiao, J. Electrochem. Soc. 162 (2015) A474–A478.
[18] D. Aurbach, E. Pollak, R. Elazari, G. Salitra, C.S. Kelley, J. Affinito, J. Electrochem. Soc. 156 (2009) A694–A702.
[19] S. Xiong, K. Xie, Y. Diao, X. Hong, J. Power Sources 246 (2014) 840–845.
[20] C. Barchasz, F. Molton, C. Duboc, J.-C. Leprêtre, S. Patoux, F. Alloin, Anal. Chem. 84 (2012) 3973–3980.
[21] Y.X. Ren, T.S. Zhao, M. Liu, P. Tan, Y.K. Zeng, J. Power Sources 336 (2016) 115–125.
[22] M. Cuisinier, P.E. Cabelguen, B.D. Adams, A. Garsuch, M. Balasubramanian, L. F. Nazar, Energy Environ. Sci. 7 (2014) 2697–2705.
[23] C.-W. Lee, Q. Pang, S. Ha, L. Cheng, S.-D. Han, K.R. Zavadil, K.G. Gallagher, L. F. Nazar, M. Balasubramanian, ACS Cent. Sci. 3 (2017) 605–613.
[24] M.A. Lowe, J. Gao, H.D. Abruña, RSC Adv. 4 (2014) 18347–18353.
[25] G. Zhang, H.-J. Peng, C.-Z. Zhao, X. Chen, L.-D. Zhao, P. Li, J.-Q. Huang, Q. Zhang, Angew. Chem. Int. Ed. 57 (2018) 16732–16736.
[26] L. Lodovico, A. Varzi, S. Passerini, J. Electrochem. Soc. 164 (2017) A1812–A1819.
[27] T. Yim, M.-S. Park, J.-S. Yu, K.J. Kim, K.Y. Im, J.-H. Kim, G. Jeong, Y.N. Jo, S.-G. Woo, K.S. Kang, I. Lee, Y.-J. Kim, Electrochim. Acta 107 (2013) 454–460.
[28] Q. Zou, Y.-C. Lu, J. Phys. Chem. Lett. 7 (2016) 1518–1525.
[29] M. Cuisinier, C. Hart, M. Balasubramanian, A. Garsuch, L.F. Nazar, Adv. Energy Mater. 5 (2015), 1401801.
[30] H. Pan, X. Wei, W.A. Henderson, Y. Shao, J. Chen, P. Bhattacharya, J. Xiao, J. Liu, Adv. Energy Mater. 5 (2015), 1500113.
[31] K. Ueno, J.-W. Park, A. Yamazaki, T. Mandai, N. Tachikawa, K. Dokko, M. Watanabe, J. Phys. Chem. C 117 (2013) 20509–20516.
[32] F.Y. Fan, Y.-M. Chiang, J. Electrochem. Soc. 164 (2017) A917–A922.
[33] R. Elazari, G. Salitra, A. Garsuch, A. Panchenko, D. Aurbach, Adv. Mater. 23 (2011) 5641–5644.
[34] E. Markevich, G. Salitra, A. Rosenman, Y. Talyosef, F. Chesneau, D. Aurbach, J. Mater. Chem. A 3 (2015) 19873–19883.
[35] R. Xu, J. Lu, K. Amine, Adv. Energy Mater. 5 (2015) 1500408–n/a.
[36] M. Hagen, P. Schiffels, M. Hammer, S. Dörfler, J. Tübke, M.J. Hoffmann, H. Althues, S. Kaskel, J. Electrochem. Soc. 160 (2013) A1205–A1214.
[37] J. Guo, X. Du, X. Zhang, F. Zhang, J. Liu, Adv. Mater. 29 (2017) 1700273–n/a.
[38] K.H. Wujcik, D.R. Wang, T.A. Pascal, D. Prendergast, N.P. Balsara, J. Electrochem. Soc. 164 (2017) A18–A27.
[39] R. Dominko, M.U.M. Patel, V. Lapornik, A. Vizintin, M. Koželj, N.N. Tušar, I. Arčon, L. Stievano, G. Aquilanti, J. Phys. Chem. C 119 (2015) 19001–19010.
[40] M. Cuisinier, P.-E. Cabelguen, S. Evers, G. He, M. Kolbeck, A. Garsuch, T. Bolin, M. Balasubramanian, L.F. Nazar, J. Phys. Chem. Lett. 4 (2013) 3227–3232.
[41] X. Liang, C. Hart, Q. Pang, A. Garsuch, T. Weiss, L.F. Nazar, Nat. Commun. 6 (2015) 5682.
[42] X. Yang, X. Gao, Q. Sun, S.P. Jand, Y. Yu, Y. Zhao, X. Li, K. Adair, L.-Y. Kuo, J. Rohrer, J. Liang, X. Lin, M.N. Banis, Y. Hu, H. Zhang, X. Li, R. Li, H. Zhang, P. Kaghazchi, T.-K. Sham, X. Sun, Adv. Mater. 31 (2019), 1901220.
[43] T.A. Pascal, K.H. Wujcik, D.R. Wang, N.P. Balsara, D. Prendergast, Phys. Chem. Chem. Phys. 19 (2017) 1441–1448.
[44] Y.-S. Su, Y. Fu, T. Cochell, A. Manthiram, Nat. Commun. 4 (2013) 2985.
[45] W. Shin, J. Lu, X. Ji, Carbon Energy 1 (2019) 165–172.
[46] C.S. Johnson Jr., Prog. Nucl. Magn. Reson. Spectrosc. 34 (1999) 203–256.

Dr. Hui Wang is currently a postdoc (JCESR I/II) in the Battery Materials and Systems group at Pacific Northwest National Laboratory. He received his Ph.D. in Materials Science & Engineering from Mie University (2014), Japan, and then became a battery program researcher under the ALCA-SPRING (JST, Japan). He specializes in the development of electrolytes and electrode materials and the regulation of the interphase chemistry for post/beyond Lithium ion batteries.

Dr. Yuyan Shao received his Ph.D. from Harbin Institute of Technology. He is a Senior Scientist at the US DOE Pacific Northwest National Laboratory. His research is focused on fundamental study and high-performance functional materials for electrochemical energy conversion and storage, including fuel cells, batteries, etc. He is named Clarivate Analytics/ Thomson Reuters Highly Cited Researcher (2014, 2017, 2018, 2019). He is an author on over 150 publications.

Dr. Huilin Pan received her PhD degree in condensed matter physics from Institute of Physics Chinese Academy of Sciences. Dr. Pan has been working on energy storage materials and systems since 2010. Her current research is primarily engaged in the design of solid electrolyte interface and the precise control and prediction of physiochemistry reactions in energy storage systems, including aqueous zinc batteries and non-aqueous sodium ion batteries.

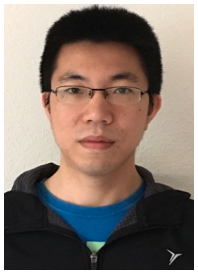

Dr. Xuefei Feng obtained his Ph.D. degree from University of Science and Technology of China in 2014. After graduation, he used to be a postdoc at Shanghai Institute of Microsystem and Information Technology, Chinese Academy of Sciences. In 2016, Xuefei Feng joined Advanced Light Source, Lawrence Berkeley National Laboratory as a postdoc and now he is a project scientist at ALS. His research interest is scientific instrument development for in-situ/operando soft X-ray spectroscopic study on energy materials.

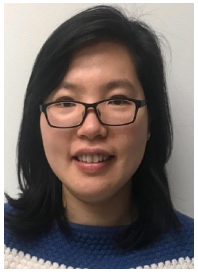

Dr. Ying Chen received her Ph.D. in Chemistry from Virginia Tech in 2015 and has since worked in Pacific Northwest National Laboratory as a postdoc and then materials scientist. Her research focuses on using solid-state NMR, solution NMR, and EPR to study a variety of materials.

Dr. Yi-Sheng Liu is a project scientist at the Advanced Light Source, Lawrence Berkeley National Laboratory. His research interest is in studying energy materials through in-situ and ex-situ soft X-ray spectroscopies. He is also dedicating to the development of in-situ soft X-ray capabilities applied to energy materials especially for metal ion batteries and hydrogen storage.

Dr. Eric Walter is a research scientist at the Environmental Molecular Sciences Laboratory located at Pacific Northwest National Laboratory. He specializes in the development and application of in situ EPR and NMR techniques to solve energy related problems, in fields such as batteries, geochemistry and catalysis.

Mark engelhard is a Senior Research Scientist at the Environmental and Molecular Sciences Laboratory located at Pacific Northwest National Laboratory. His expertise is in the use of X-ray photoelectron spectroscopy to study surface and interphase chemistry. He has published over 500 papers and his Web of Science *h* index is 85, He has been named a Highly Cited Researcher by Clarivate Analytics in 2018 & 2019 and has been honored with several awards, including the US Department of Energy's award for outstanding scientific accomplishment in Materials Chemistry, AVS George T. Hanyo award in 1997 and elected AVS Fellow in 2013.

Dr. Kee Sung Han is a Research Scientist at Pacific Northwest National Laboratory. He received his Ph.D. in 2006 from Konkuk University, Seoul, South Korea, in Solid-State Physics. He did his postdoctoral training specializing in Nuclear Magnetic Resonance (NMR) Spectroscopy from Pacific Northwest National Laboratory, Oak Ridge National Laboratory, and Korea Basic Science Institute. His current research is focused on characterization of energy storage materials and electrochemical phenomena in energy storage systems using NMR techniques including pulsed-field gradient (PFG) diffusion NMR. He is also interested in applications of solid-state NMR to various areas in materials science.

Tao Deng is currently a PhD candidate in the Department of Chemical and Biomolecular Engineering at University of Maryland-College Park. He received his bachelor's degree from Tianjin University (2014) and M.Sc. degree from Rice University (2016). His research interests focus on electrochemistry and interface chemistry for high-energy Li/Na metal batteries.

Guoxi Ren received his BE degree in New Energy Materials and Devices from Hefei University of Technology, China in 2015. He is now pursuing his PhD degree in Prof. Xiaosong Liu's group at Shanghai Institute of Microsystem and Information Technology, Chinese Academy of Sciences, China. His current research interests focus on solid electrolytes and all-solid-state Li-ion batteries studies via synchrotron X-ray characterizations.

Dr. Dongping Lu is a materials scientist in the Battery Materials and Systems group at Pacific Northwest National Laboratory (PNNL). Dr. Lu's research interest is material and electrolyte development for energy storage as well as in-depth mechanism analysis through advanced in-situ/ex-situ techniques. Currently, he is focusing on the development of high energy lithium-sulfur including new materials, fundamental understanding, and pouch cell design and demonstration. He received his Ph.D. in Physical Chemistry (Electrochemistry) at Xiamen University, China in 2011. Dr. Lu has more than 40 papers published in peer-reviewed professional journals and holds 6 granted and pending U.S. Patents.

Dr. Xiaochuan Lu is currently an Associate Professor in the Department of Applied Engineering Technology at North Carolina A&T State University (NC A&T). His research interests include Na batteries, Li-ion batteries, redox flow batteries, and solid-state electrolytes. Prior to joining NC A&T, he was working at Pacific Northwest National Laboratory as a Senior Research Scientist for over eleven years. Dr. Lu has published over 60 papers in peer reviewed journals, 2 book chapters, and 10 U S. patents (including pending). He received his Ph.D. degree in Mechanical Engineering at Tennessee Technological University in 2008.

Dr. Wu Xu is currently a Chief Scientist in Energy and Environment Directorate at Pacific Northwest National Laboratory (PNNL). Before joining PNNL, he worked as a Senior Scientist in Ferro Corporation and a Faculty Research Associate in Department of Chemistry and Biochemistry at Arizona State University. Dr. Xu received his Ph.D. in chemistry from National University of Singapore, Singapore. His research interests include the development of electrolytes and electrode materials and the investigation of electrode/electrolyte interphases for various energy storage systems. Dr. Xu has published over 180 papers, 1 book, 6 book chapters, and 31 U S. patents granted.

Dr. Chunsheng Wang is a Robert Franklin and Frances Riggs Wright Distinguished Chair Professor in the Department of Chemical & Biomolecular Engineering & Chemistry and Biochemistry at the University of Maryland. He is an associate editor of ACS Applied Energy Materials, and UMD Director of The UMD-ARL Center for Research in Extreme Batteries. His research focuses on rechargeable batteries. He has published more than 270 papers. Dr. Wang is a Highly Cited Researcher of 2018 and 2019, with more than 21000 citations and H-index of 76 (ISI).

Dr. Jun Feng is a professor at the department of material science and engineering and Institute for quantum science and engineering of Southern University of Science and Technology in China since 2020. He joined the division of Advanced Light Source of Lawrence Berkeley National Laboratory as a tenure scientist between 1998 and 2020. His current research interests focus on novel energy science, novel photocathode materials, high brightness electron source, ultrafast science, quantum electron microscopy, synchrotron radiation, free electron laser and their applications.

Dr. Karl Mueller is a physical chemist, who currently serves as the Chief Science and Technology Officer for the Physical and Computational Sciences Directorate at PNNL. He is also a Laboratory Fellow, and his primary scientific research focuses on the development and utilization of nuclear magnetic resonance (NMR) techniques. Dr. Mueller and his research team are studying a range of fundamental scientific problems in advanced energy storage as part of the Joint Center for Energy Storage Research (JCESR), where he is also the Lead Scientist for the Charge Transfer at Dynamic Interfaces research thrust.

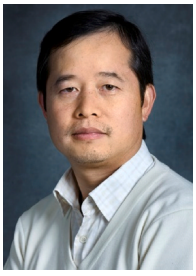

Dr. Jinghua Guo is a Senior Scientist at the Advanced Light Source, Lawrence Berkeley National Laboratory and Adjunct Professor in the Department of Chemistry and Biochemistry, University of California at Santa Cruz. His research interest focuses soft x-ray spectroscopic characterization of nanostructured and energy materials, interfacial phenomena, electrochemistry, catalysis and chemical transformation. He has developed instrumentation for the in-situ/operando soft x-ray spectroscopy and enabled the study of energy and functionalized materials in real-world conditions. He has published over 430 peer-reviewed articles.

Dr. Kevin R. Zavadil is a Distinguished Member of Technical Staff in the Material, Physical and Chemical Sciences Center at Sandia National Laboratories (USA). He received his Ph.D. in Chemistry from the University of Arizona in 1989. He manages one of five science thrust research portfolios for the Joint Center for Energy Storage Research (JCESR), a US DOE Energy Innovation Hub. His current research is focused on the material and interfacial science of electrochemical energy storage devices, including lithium and multivalent metal batteries and redox flow batteries.

Dr. Ji-Guang (Jason) Zhang is a Laboratory Fellow of the Pacific Northwest National Laboratory. He is the group leader for PNNL's efforts in energy storage for transportation applications and has 26-year experience in the development of energy storage devices, including Li-ion batteries, Li-metal batteries, Li-air batteries, Li–S batteries, and thin-film solid-state batteries. He was the co-recipient of two R&D 100 awards, holds 30 patents (with another 28 patents pending) and publishes more than 300 papers in refereed journals. He was named Highly Cited Researchers since 2015 in Materials Science.